Postprint *International Journal of Heat and Mass Transfer* Vol. **130**, pp. 946-959 (2019)
https://doi.org/10.1016/j.ijheatmasstransfer.2018.10.138

Vortical flow patterns by the cooperative effect of convective and conductive heat transfers in particle-dispersed natural convection

Jingchen Gu[1], Shintaro Takeuchi[1*], Toshiaki Fukada[2] and Takeo Kajishima[1]

[1] Department of Mechanical Engineering, Osaka University
2-1 Yamada-oka, Suita-city, Osaka 565-0871 Japan
[2] Central Research Institute of Electric Power Industry
2-6-1 Nagasaka, Yokosuka, Kanagawa 240-0196, Japan
* Corresponding author: shintaro.takeuchi@mech.eng.osaka-u.ac.jp

Abstract

Cooperative effect of the conductive and convective heat fluxes on the development of vortical structures is studied in a particle-dispersed natural convection. A numerical approach is proposed that visualises the heat transfer paths through the fluid and finite-volume particles (i.e., non-point particles) to show the spatial extension of the heat fluxes and its influence on the flow field. The approach is applied to a weakly-convective dense particulate system under the Rayleigh number 10^5 containing more than 4000 particles (solid volume fraction 42.8 %) of various conductivities. With highly-conductive particles (in comparison to the ambient fluid), local downward convection of a large-scale vortical flow strengthens the conductive heat flux near the bottom hot wall in the counter-convective direction by the increase of the vertical temperature gradient, and the observation of the spatial extension of the heat flux lines indicates that the increase of the solid volume fraction near the hot wall further strengthens the conductive heat flux. The paired upward convection causes strengthened conductive heat flux near the top cold wall by the same increase mechanism. The above interplay of the local heat fluxes in the dense solid-dispersed media are found to influence on the formation and transition of the large-scale vortical structures through the distribution of the moment of buoyancy in a horizontal plane. An analytical model for a low-dimensional vortex system shows that buoyancy gradient and vorticity diffusion could determine the time-development of the large-scale vortical structure.

Key words: Dense particle-laden flow; Vortical structure; Inhomogeneous media; Heat transfer; Conduction; Convection.

1 Introduction

Heat transfer in dense particulate flows is observed in industrial applications including energy conversions and chemical processes. Several studies investigated the mechanism of heat transfer in particulate media by experiments [1, 2, 3] and numerical simulations [4, 5, 6]. In the earlier study, Michaelides [7] mentioned that the presence of the particles contributes to increase the heat transfer coefficient of the particulate flows due to enhancement of convection. The above studies suggest the importance of the behaviour of individual particles on the heat transfer.

To study the effect of the convection on the heat transfer in a particle-laden flow, Murray et al. [8] experimentally revealed that, by strengthening the local convection over the front of a heated cylinder in a cross flow, the dispersed particles enhanced the heat transfer due to the increase of the thermal capacity

of the suspension. Murray [9] further studied the same case by including the local effect of particle-wall conduction into the analysis and suggested that the rebound of the dispersed particles at the heated surface enhanced the local heat transfer and the convective component of the heat flux as well as the inter-particle heat transfer.

The effect of the conduction on the net heat transfer in a suspension has also been investigated in the past [10, 11, 12]. Mansoori et al. [11] simulated the heat transfer in a particulate flow through a vertical pipe with a constant wall heat flux. They found that the conduction due to the inter-particle contact significantly affects the heat transfer in the suspension, particularly at high mass loading ratios. In their sequel work [12], they showed that the effect of the particle-particle conduction was more significant for smaller particles and lower Reynolds number. Their findings agree with the result by Avila and Cervantes [10], who investigated the heat transfer in turbulent particulate pipe flow: they showed that the flow Reynolds number, the particle loading ratio and the particle diameter are the influential parameters on the conduction in the particulate media. The experimental study of Mansoori et al. [2] also supports the results obtained by Avila and Cervantes [10] and Mansoori et al. [11, 12].

On the other hand, catalyst engineers studied the heat transfer by a flow passing around a fixed conductive particle and through the inter-particle spacings [13, 14], as a catalyst particle could encounter meltdown depending on its surrounding gas flow and the particle size [15]. The studies revealed the significance of the conduction from the wall or heat source in the particle and of the characteristic flow patterns in the particle-wall and inter-particle regions.

The above studies suggest that a separate study of either the convective or conductive heat transfer does not always provide the entire picture of the heat transfer in the particulate flow. To analyse the mechanism of the heat transfer in an inhomogeneous media, the interactive mode of the conductive and convective heat fluxes should be focused via the flow structure. Our previous studies showed that the effect of the finite-volume particles on the heat transfer is significant when the particle is more conductive than the ambient fluid [16, 17, 18, 19]. Understanding the cooperative effect between the conductive and convective heat transfers and the effects on the flow structure provides significant insights/perspectives for the heat exchange by the flow controls in a dense media containing finite-volume particles.

Under intense conductive or convective heat flux, decomposition of the heat flux into those components would be helpful for visualising and understanding the global heat transfer mechanism. In the present study, heat flux lines (HFLs) by conduction and convection are introduced to investigate the instantaneous heat transfer by both fluid and particle phases, and the interplay between those fluxes is studied in three dimensions. To facilitate the numerical simulation of moving particles in a fluid, an Eulerian-Lagrangian formulation on a fixed-mesh is employed. The fluid-particle interaction problem is solved by an original immersed solid method [18, 20] by resolving one particle diameter with ten grid points. The temperature field is also solved on the Eulerian frame of the same spatial resolution to solve the local heat transfer events such as the interfacial heat transfer and the thermal contact resistance [16, 18]. The above treatments and methods for the fluid-particle interaction and heat transfer are particularly developed for finite-volume particles, and the numerical methods are capable of handling the convective and conductive heat fluxes in a particle-dispersed flow, including the heat transfer inside a particle. We study interactive modes of the conductive and convective heat fluxes by visualising the instantaneous HFLs for several cases with different particle conductivities and show the effect of the moment of buoyancy on the large-scale vortical flow. Through a simplified low-dimensional vortex model, a transition of large-scale vortical structure is discussed.

2 Governing equations and outline of the computational method

The fluid phase is assumed to be an incompressible Newtonian fluid with constant density and viscosity. The governing equations for the fluid phase are the equations of continuity, momentum and energy given by the following equations in non-dimensional form:

$$\nabla \cdot \boldsymbol{u} = 0 \,, \tag{1}$$

$$\frac{\partial \boldsymbol{u}}{\partial t} + (\boldsymbol{u} \cdot \nabla)\boldsymbol{u} = -\nabla p + \sqrt{\frac{\mathrm{Pr}}{\mathrm{Ra}}}\nabla^2 \boldsymbol{u} - (T - T_0)\boldsymbol{j} \,, \tag{2}$$

$$\frac{\partial T}{\partial t} + (\boldsymbol{u} \cdot \nabla)T = \frac{1}{\sqrt{\mathrm{Pr}\,\mathrm{Ra}}}\nabla^2 T \,, \tag{3}$$

where $\boldsymbol{u}$ is the fluid velocity, t the time, p the pressure, T the temperature, T_0 the reference temperature, $\boldsymbol{j}$ the unit vector in the direction of gravity. Here, Prandtl number and Rayleigh number are defined as $\mathrm{Pr} = \mu c/\lambda$ and $\mathrm{Ra} = \mathrm{Pr} \cdot \rho U H/\mu$, respectively, where μ is kinetic viscosity, c the specific heat, λ the thermal conductivity, ρ the density, $U = \sqrt{\beta g\, \Delta T H}$ the reference velocity, H the reference length, β the volumetric thermal expansion coefficient, g the magnitude of the gravitational acceleration and ΔT the characteristic temperature difference. The reference pressure is ρU^2.

The computational method is briefly explained. Our original immersed solid method [20] is employed for the momentum exchange between the solid and fluid phases, and a two-stage time-marching method [18] for the fluid and particle phases is used. Temperature gradient within the particles is taken into account through an interfacial heat flux model [16] on the Eulerian frame. For the particle-particle and particle-wall collision, a discrete element model with soft-sphere collision [21] is used, and an inter-particle heat transfer model [18] is applied upon contact. More details about the numerical method are given in Appendix A. Both fluid-particle coupling and heat transfer solvers have been fully validated through comparisons with analytical and reference numerical solutions for several problems such as particle migration in a sheared flow [18], heat conduction through bi-layered material and heat transport in a closed domain [16, 17].

Hereafter, the subscripts "s" and "f" for the above variables denote the solid and fluid phases, respectively.

3 Convective and conductive heat flux lines (HFLs)

We introduce a method that characterises heat transfer in a particulate flow. As Gu et al. [19] suggested, the local heat transfer at the particle surface is of importance as it determines the conductive and convective heat transfers by the particle. The present numerical method handles those heat transfer components (with no empirical model) by taking account of the interfacial conditions of the heat flux at the fluid-solid interface [16, 22] as well as inter-particle contact [18]. Along with the numerical tool, the conductive heat flux line (HFL) has been found to be an effective index [19] to trace the instantaneous heat transfer at the same scale as the particle diameter. In the present study, both conductive and convective HFLs are introduced for studying the coupled effect by the heat flux and vortical structure.

HFL is an analogy of streamlines and defined as a set of line-segments tangent to the local (convective and conductive components of) heat flux vectors:

$$\frac{\mathrm{d}x}{\rho c T u} = \frac{\mathrm{d}y}{\rho c T v} = \frac{\mathrm{d}z}{\rho c T w} \tag{4a}$$

$$\frac{\mathrm{d}x}{-\lambda \partial T/\partial x} = \frac{\mathrm{d}y}{-\lambda \partial T/\partial y} = \frac{\mathrm{d}z}{-\lambda \partial T/\partial z} \,, \tag{4b}$$

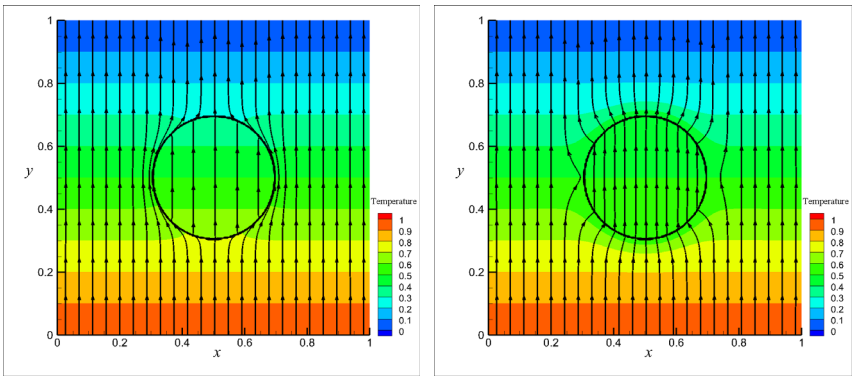

(a) $\lambda_s/\lambda_f = 10^{-2}$ (b) $\lambda_s/\lambda_f = 10^{2}$

Figure 1: Conductive heat flux lines around and inside a 2-D (a) poorly conductive particle and (b) highly-conductive particle after reaching steady state. The particle is fixed in the centre of a square domain and a constant temperature difference is imposed along the y axis.

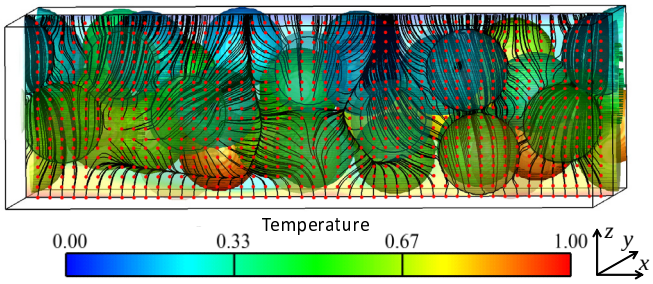

Figure 2: Example of the conductive HFLs based on a 3-D simulation result. The computational condition is the same as Case B2 in Gu et al. [19]: $\mathrm{Ra} = 10^5, \lambda_s/\lambda_f = 10^2$, the number of particle $n_p = 92$ and the corresponding solid volume fraction is 42.8%. The HFLs are integrated from the points arranged at constant intervals in the xz plane shown by dotted symbol, and the three dimensional HFLs are projected onto the vertical plane.

Table 1: The non-dimensional parameters

Prandtl number	Pr	1.0
Rayleigh number	Ra	10^5
Density ratio	ρ_s/ρ_f	1.0
Specific heat ratio	c_s/c_f	1.0
Ratio of thermal expansion rate	β_s/β_f	1.0

where u, v and w are the velocity components in the x, y and z directions, respectively.

Figure 1 shows two typical examples of conductive HFLs around and inside a particle of different heat conductivities fixed in a natural convection confined in a square box. A constant temperature difference is imposed along the y axis. For the case with the poorly-conductive particle ($\lambda_s/\lambda_f = 10^{-2}$), the HFLs are mainly go around the particle and only a small number of HFLs go through the particle, whereas the highly-conductive particle ($\lambda_s/\lambda_f = 10^2$) draws the HFLs into the particle and a characteristic hour-glass shape of the HFLs is formed. For more detail, see Appendix B. As the conductive HFLs shown in Fig. 2, the HFLs enable visualisation of the transport of heat inside as well as around the finite-volume particles, passing through the contacting sites of the particles and nearly-contacting inter-particle spacings.

4 Results and discussion

4.1 Computational conditions and Nusselt number

A dense particle-dispersed natural convection is simulated under an unstable temperature stratification between two parallel walls. Figure 3 shows a schematic of the computational domain and the initial particle arrangement on the centres and vertices of the body-centred cubic (bcc) units. Hereafter, the vertical height of the domain H is chosen as the reference length. The dimensions of the domain are $L/H = W/H = 3.2$ in the horizontal x and y directions, respectively. The periodic boundary condition is applied in the horizontal directions. The number of grid points in both horizontal directions is 256, and 80 points are arranged in the vertical (z) direction. The temperature of the upper wall is set to $T_c = 0$, and the temperature difference between the lower and upper walls are kept constant to be $T_h - T_c = \Delta T$.

The solid particles are assumed to be rigid sphere of a uniform size, and one particle diameter is discretised with 10 grid points, $D_p/\Delta = 10$, where D_p is the particle diameter and Δ is the grid size.

Our previous study [19] on the heat transfer in the dense particulate flow shows that the highly-dense condition (the solid volume fraction 54%) attenuated the convection (unlike the less-dense cases such as 30.8% and 42.8%) even under a high Rayleigh number, resulting in the decrease in the net heat flux in the particle-dispersed flow. For this reason, we choose the bulk solid volume fraction to be an intermediate value of 42.8 % and $\mathrm{Ra} = 10^5$ in the present study, as the roles of the conductive and convective heat fluxes on the net heat transfer was remarkable under the moderate intensity of the convection of the fluid and particles. The ratio of the thermal conductivity λ_s/λ_f is fixed to be 10^2, unless specified otherwise. Initially, the fluid and particles are stationary, and the temperature $T = 0$ is given in the entire domain. The particles are arranged at the constant intervals in the respective directions (i.e., on the vertices of the bcc units), as shown in Fig. 3, and half of the centre-positions of the bcc units are filled with the particles: with the number of particles on the bcc vertices $n_L = n_W = 21$ and $n_H = 7$ in the respective directions, the total number of particles in the domain is $n_p = n_L n_W n_H + (n_L - 1)(n_W - 1)(n_H - 4) = 4287$.

The other computational parameters are summarised in Table 1.

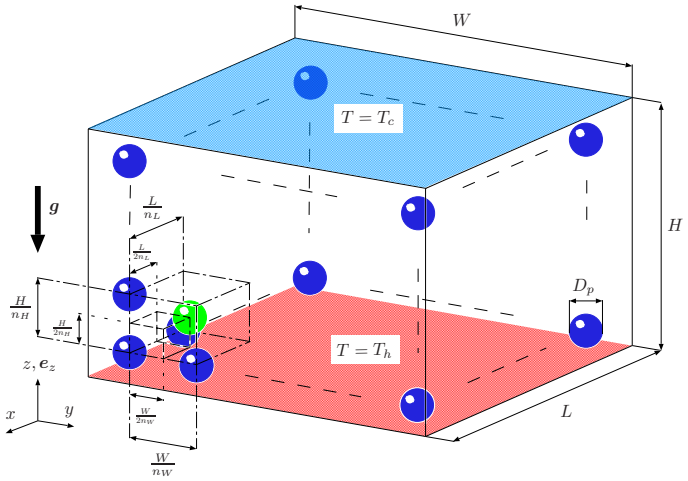

Figure 3: Schematic of the computational domain and the initial arrangement of particles. The particle are placed at the vertices and the centres of the body-centred cubic (bcc) units. The number of particles in the x, y and z directions are n_L, n_W and n_H, respectively, and half of the bcc centres are filled with the particles in the present study.

The heat transfer is evaluated by the following horizontally-averaged Nusselt numbers:

$$\mathrm{Nu_d}(t,z) = \frac{1}{\lambda_f \Delta T}\frac{H}{LW}\int_0^W\int_0^L \lambda\left(-\frac{\partial T}{\partial z}\right)\mathrm{d}x\mathrm{d}y\,, \tag{5}$$

$$\mathrm{Nu_v}(t,z) = \frac{1}{\lambda_f \Delta T}\frac{H}{LW}\int_0^W\int_0^L \rho c T\boldsymbol{u}\cdot\boldsymbol{e}_z\,\mathrm{d}x\mathrm{d}y\,, \tag{6}$$

$$\mathrm{Nu}(t,z) = \mathrm{Nu_d}(t,z) + \mathrm{Nu_v}(t,z)\,, \tag{7}$$

where $\mathrm{Nu_d}$ and $\mathrm{Nu_v}$ are the conductive and convective contributions in the Nusselt number, respectively. The local thermal conductivity λ includes the effects of the interface between the fluid and particles as well as the thermal contact resistance at the inter-particle and particle-wall contacting sites [18, 19].

Figure 4 shows some examples of the time evolutions of Nu on the top and bottom walls in a natural convection of $\mathrm{Ra} = 10^5$: Figs.4(a) and 4(b) are the cases with poorly and highly conductive particles, respectively. Due to the initial condition, Nu is initially large on the lower wall (red line) and equals to 0 on the upper wall (blue line). After the non-dimensional times $tU/H = 150$ and 80 for the cases of $\lambda_s/\lambda_f = 10^{-2}$ and 10^2, respectively, the Nu values on the lower and upper walls tend to show negligible difference, and then, we regard that the flow reaches fully-developed. Hereafter, we discuss the heat flux and suspension flow only in fully-developed state to exclude the effect of the initial condition.

The time histories of $\mathrm{Nu_d}(t, H/2)$ / $\mathrm{Nu}(t, H/2)$ are also plotted in Fig. 4. For the case with the poorly-conductive particles, the heat transfer is mainly by the convection, whereas the case with the highly-conductive particles shows that the conductive and convective contributions in the Nusselt number are in the same order of magnitude. The above result coincides with the observation by Tsutsumi et al. [17] that the effect of particle conductivity appears as additional Nusselt number on the Nusselt number of the single phase flow ($n_p = 0$). This phenomenon is understood that the highly-conductive particles enhance the convection by quick adoption to the local temperature environment, whereas the poorly-conductive particles induce a weak convection by the hindrance of the heat transfer from/to the hot/cold wall to/from the fluid. However, by increasing the highly-conductive particles to the solid volume fraction of 54%, the development of the convection is hampered and the contribution by the conduction becomes overwhelming [19].

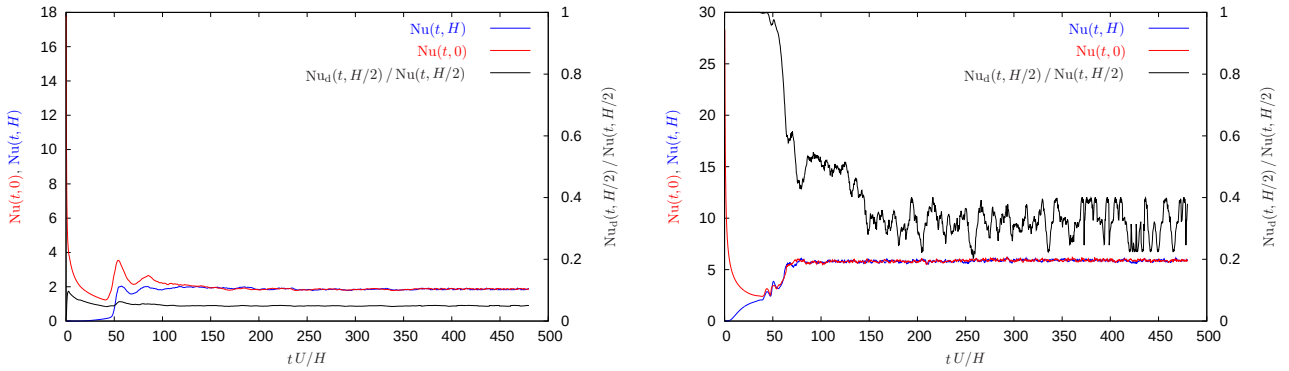

(a) $\lambda_s/\lambda_f = 10^{-2}$ (b) $\lambda_s/\lambda_f = 10^{2}$

Figure 4: The time history of Nusselt number (Nu) under $\mathrm{Ra} = 10^5$ for two different particle conductivities; (a) $\lambda_s/\lambda_f = 10^{-2}$ (b) $\lambda_s/\lambda_f = 10^{2}$. The bulk solid volume fraction is 42.8 % (the particle number is 4287).

4.2 The conductive and convective heat fluxes with particles of $\lambda_s/\lambda_f = 10^2$

Figures 5(a) and 5(b) visualise the instantaneous conductive and convective HFLs, respectively, at $tU/H = 480$, and the cross-sectional temperature field at $y/H = 0.5$ is shown in Fig. 5(c). The conductive HFL is coloured by the local solid volume fraction (red and blue mean the regions in the particle and fluid phases, respectively), while the convective HFL is coloured by the magnitude of the convective component of the heat flux. The particles are coloured by the local surface temperature. In the figure, the particles in the front half of the domain (i.e., $0.5 \leq y/W \leq 1.0$) are not shown to clearly visualise the HFLs. As the low temperature region extends in the $-z$ direction in the left half of Figure 5(c), the concentrated convective HFLs in Fig. 5(b) are caused by a down-flow. The paired up-flow extends in the vertically upward ($+z$) direction in the right half of the domain, and therefore, a roll vortical structure develops with its axis along the y direction.

The HFLs in Figs. 5(a) and 5(b) are drawn from the points arranged at the constant intervals in the xy planes of $z/H = 0$ (hot wall) and $z/H = 0.8$, respectively. Selecting the different starting planes for the conductive and convective HFLs is to visualise from the thermally-upstream and hydrodynamically-upstream sides, respectively, in the down-flow region, so that the spatial extensions of the both components of the heat fluxes in the vortical flow field are naturally understood in the down-flow region.

A schematic of the conductive and convective HFLs around a single-phase roll vortex is illustrated in Fig. 6. Note that, in the down-flow region, a fluid of low temperature ($T' = T - \langle T \rangle < 0$) convected by a downward velocity component ($w' = w - \langle w \rangle < 0$) generates positive convective heat transfer ($w'\,T' > 0$), where $\langle T \rangle = \Delta T(1 - z/H)$ and $\langle w \rangle = 0$. The downward and upward convections strengthen the local temperature gradient near the hot and cold walls, respectively, as confirmed by the contour of the temperature in the xz cross-section (Fig. 5(c)).

The net heat transfer rate is determined by the vortex structure with the aid of the transportation of the particles. A typical motion of the particles in the roll cell of Fig. 5 is as follows: the particles cooled by the upper wall descend to the lower wall by the down-flow, travel horizontally in the near-wall region until those are heated by the lower wall, and finally ascend to the upper wall by the up-flow. The particles transported by the down-flow generate a relatively dense region near the lower wall, as confirmed by the colour scale depicted on the conductive HFLs in Fig. 5(a). The down-flow collects the conductive HFLs stemming from a wide area on the bottom hot wall, giving rise the increase in the local conductive component of the heat flux near the lower wall, as the conductive HFLs mainly go through inside the particles. However, in the middle level (i.e., in the region away from the walls), the conductive HFLs suddenly change the pass

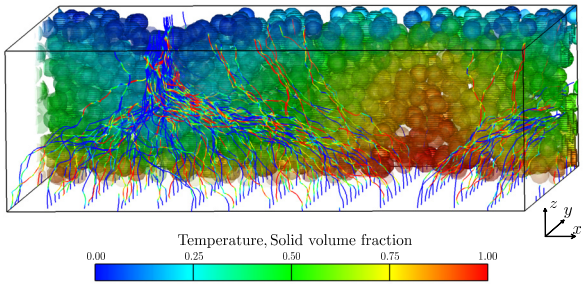

(a) Conductive HFLs

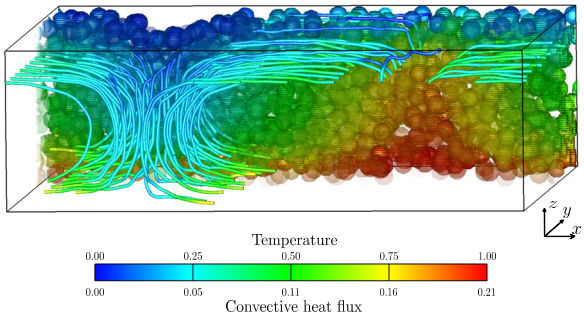

(b) Convective HFLs

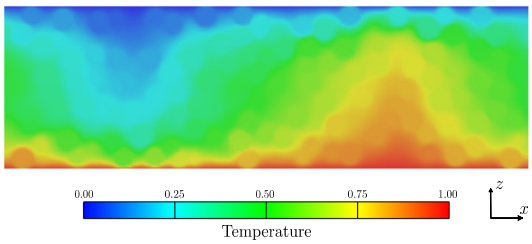

(c) Cross-sectional temperature

Figure 5: Instantaneous view of the heat flux lines at $tU/H = 480$ highlighting the down-flow. (a) Conductive and (b) convective heat flux lines (HFLs), and (c) the cross-sectional temperature field at $y/W = 0.5$. The particles are shown only in the rear half of the domain ($0.5 \leq y/W \leq 1$), and the colour on the particles means the local surface temperature. The colours on the lines represent (a) the local solid volume fraction and (b) the convective heat flux.

through the fluid-filled region, as the blue colour on the HFLs suggests, due to relatively loosely-packed environment with less opportunity of the inter-particle contact heat transfer.

Figure 7 visualises the HFLs associated with the up-flow at the same instant as Fig. 5. The conductive and convective HFLs are depicted from the upper wall and near-lower-wall region ($z/H = 0.2$), respectively. The conductive HFLs calculated from the upper wall mean that the HFLs ending at the upper wall (i.e., thermally-downstream side) are retrieved in the thermally-upstream side (i.e., backward retrieval) in order to identify the characteristic heat transfer paths and heat source location. The up-flow generates a region of weaker temperature gradient near the bottom wall (the right-hand side of Fig. 5(c)), giving rise a relatively weak amount of conductive heat flux from a limited area on the hot wall as shown in Fig. 7(a), which is upside-down to the conductive HFLs in Fig. 5(a).

Both Figs. 5 and 7 show that the down-/up-flow convection causes the increase in the temperature gradient near the bottom/top wall, giving rise the increase in conductive flux. This basic cooperative effect is even pronounced by the particles in the locally-dense region by making up the "passage" of the conductive HFLs between the (touching or nearly-touching) particles, as shown in Fig. 2.

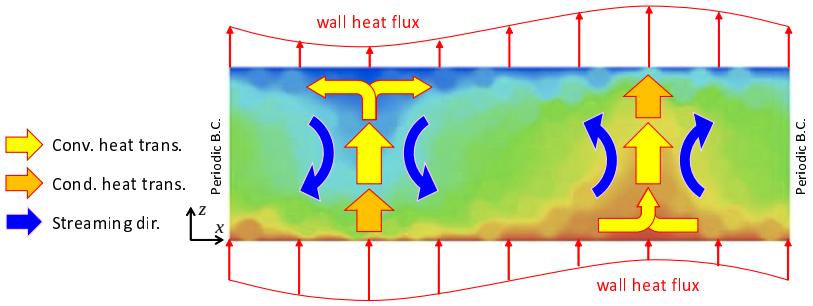

Figure 6: Schematic of the conductive and convective heat fluxes around a single-phase roll vortex in association with the up- and down-flows and wall heat flux. Arrows indicate the directions of the heat flux and convection depicted over the temperature contour of Fig. 5(c).

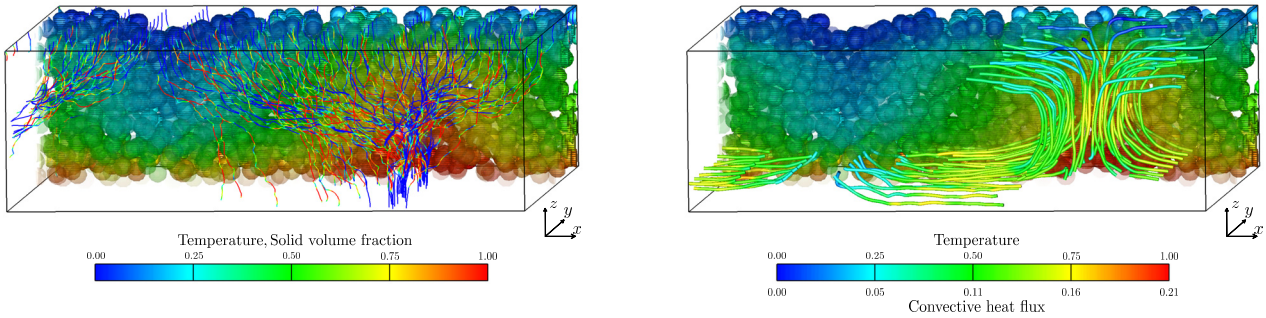

(a) Conductive HFLs

(b) Convective HFLs

Figure 7: Instantaneous view of the heat flux lines at $tU/H = 480$ highlighting the up-flow. (a) Conductive (backward-drawing) and (b) convective (forward-drawing) heat flux lines (HFLs) with the particles of the conductivity ratio $\lambda_s/\lambda_f = 10^2$. The colours on the lines represent (a) the local solid volume fraction and (b) the convective heat flux.

4.3 Involvement of heat transfer on the formation of flow patterns

The interplay of the conductive and convective components of the heat fluxes via the vortical structure also influences the time-development of the large-scale vortical structure. Figure 8 shows typical snapshots of the temperature distribution and the HFLs at two different instants. The conductive and convective HFLs are calculated from the points arranged in two different xy planes at $z/H = 0$ and 0.8, respectively. The particles are not shown to clearly visualise the distribution (or spatial extension) of the HFLs. A cross-section at $z/H = 0.75$ is selected to show the temperature distribution of the suspension near the upper wall. At $tU/H = 280$ (Figs. 8(a) and 8(b)), a point-sink is the characteristic large-scale structure. In the figures, a large number of conductive and convective HFLs near the hot wall show that the local heat flux by the downward convection (Fig. 8(b)) strengthens the local conduction (Fig. 8(a)) in the $+z$ direction, which is the same mechanism as Fig. 5. In the horizontal temperature profile, the local cold and hot spots are observed at the point-sink and source regions, respectively.

On the other hand, the point-source/sink structure has changed to a line-source/sink (i.e., straight-roll cell) structure by $tU/H = 480$ (Figs. 8(c) and 8(d)). Along the line-source/sink region, the strong buoyancy force induced by the local high temperature is the driving force to maintain the straight-roll cell.

International Journal of Heat and Mass Transfer Vol. **130**, pp. 946-959 (2019)
https://doi.org/10.1016/j.ijheatmasstransfer.2018.10.138

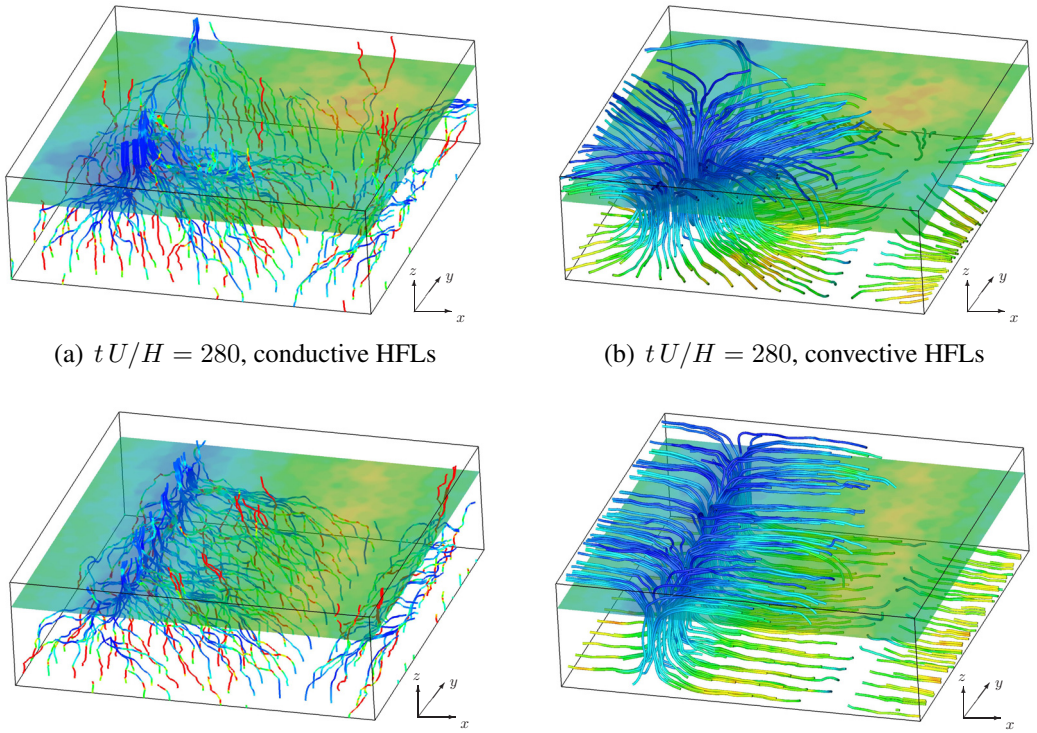

(a) $tU/H = 280$, conductive HFLs

(b) $tU/H = 280$, convective HFLs

(c) $tU/H = 480$, conductive HFLs

(d) $tU/H = 480$, convective HFLs

Figure 8: Typical snapshots of the distributions of the conductive and convective HFLs at (a)(b) $tU/H = 280$; (c)(d) $tU/H = 480$; Temperature distribution is shown in the $z/H = 0.75$ cross-section. The particles are not drawn in the figure. The colours on the lines represent (a) the local solid volume fraction and (b) the convective heat flux on the same colour scale as Fig. 5.

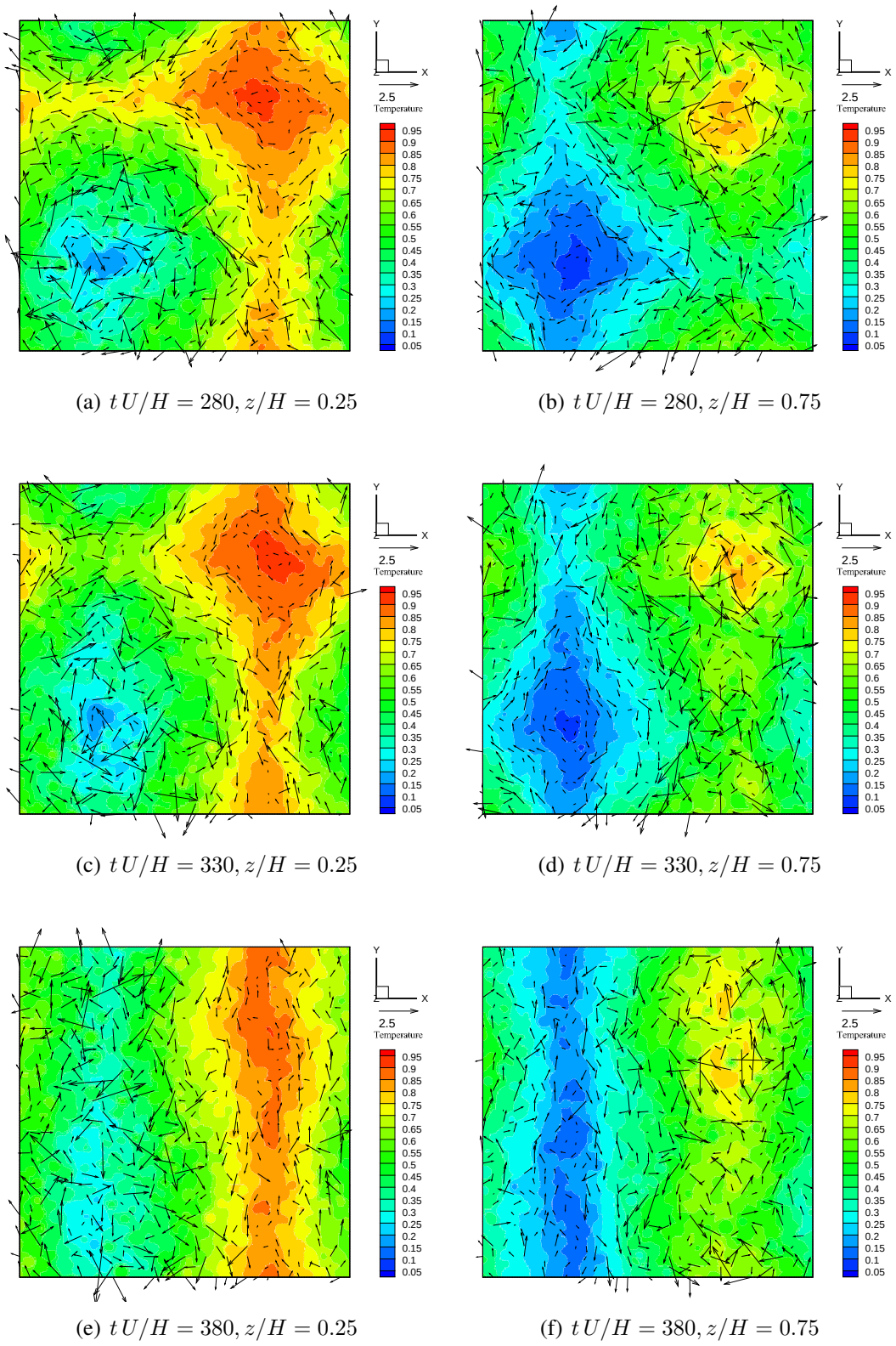

(a) $tU/H = 280, z/H = 0.25$ (b) $tU/H = 280, z/H = 0.75$

(c) $tU/H = 330, z/H = 0.25$ (d) $tU/H = 330, z/H = 0.75$

(e) $tU/H = 380, z/H = 0.25$ (f) $tU/H = 380, z/H = 0.75$

Figure 9: Distributions of the vector $\nabla \times (0, 0, T)^T$ in two horizontal planes at three different times.

The transition from a point-sink structure (at $tU/H = 280$) to a line-sink structure (at $tU/H = 480$) is understood as follows. As shown in Fig. 1(b), the conductive HFLs are likely to be drawn into the particle, forming an hour-glass shape of the conductive HFLs. In a region where the particles are densely-populated more vertically than horizontally (like a region in the down-flow or up-flow in Figs.5 and 7), the superposed hour-glass regions would reinforce the heat flux in the vertical direction, rather than horizontally, by the conduction "passage" as observed in Figs. 2 and 5(a). A simple model of the superposed effect of the conductive HFLs is explained in Appendix B. The superposed heat flux in that vertically elongated high-concentration region induces temperature-gradient field in a horizontal plane. Then, the horizontal temperature gradient results in the first-order moment of buoyancy, as shown by the following equation:

$$-\frac{g\beta}{2}\int |\boldsymbol{x}|^2 \left(\frac{\partial T}{\partial y}, -\frac{\partial T}{\partial x}, 0\right)^{\mathrm{T}} \mathrm{d}V = \int \boldsymbol{x} \times \boldsymbol{F}_{\mathrm{b}}\, \mathrm{d}V \ , \tag{8}$$

where $\boldsymbol{x}$ is the position vector from the domain centre and $\boldsymbol{F}_{\mathrm{b}} = g\beta(T - T_0)\boldsymbol{e}_z$. More detail of this equation is found in Eq.(B33) in Appendix B.

Point-source/sink structure is expected to involve strong horizontal temperature gradient, generating clockwise and counter-clockwise moment vectors around the sink and source, respectively. Interestingly, as Figs. 8(a) and 8(b) show, a germ of line-source structure already exists in the bottom region at around $x/L = 0.75$. Figure 9 shows the vectors of $\nabla \times (T\boldsymbol{e}_z)$ in two different horizontal planes together with the instantaneous horizontal temperature fields from $tU/H = 280$ to 380. On both sides of the lined-germ in Figs. 9(a) and 9(c), the vectors $\nabla \times (T\boldsymbol{e}_z)$ point in the y direction, which infers that the bottom line-source is the onset structure that emerges later as a straight-roll cell, as observed at $tU/H = 480$. Generally, the vectors tend to be tangential to the iso-temperature lines, and the disturbed vectors are the signature of the nearby particles. With an influential flow structure (like a line-source near the hot wall), the orientations of the vectors tend to align with one another. The moment of buoyancy (corresponding to the coherent arrangement of $\nabla \times (T\boldsymbol{e}_z)$ vectors with the weight of $|\boldsymbol{x}^2|$ in Eq.(8)) is a significant generating/maintaining source of large-flow structure. Therefore, part of the effect of the columnar structure of the conductive particles is understood as the source of the horizontal distribution of temperature, resulting in moment of buoyancy that induces flow structure.

Further, the particle-dispersed flow has the following subsidiary mechanisms of generating the distribution of moment of buoyancy, in comparison to a single-phase natural convection. By using the energy conservation equation (3), the source of the $\nabla \times (T\boldsymbol{e}_z)$ vector is identified in more detail as the right-hand side of the following equation:

$$\begin{aligned} \rho c \frac{\mathrm{D}}{\mathrm{D}t}\left[\nabla \times (T\boldsymbol{e}_z)\right]_i \;=\; & \frac{\partial (S_i T_k)}{\partial x_k} - \frac{\partial (S_j T_j)}{\partial x_i} + \nabla^2\left[\lambda \nabla \times (T\boldsymbol{e}_z)\right]_i \\ & -\rho c \left(\varepsilon_{ij3} d_{jk} \frac{\partial T}{\partial x_k} - \frac{1}{2}\omega_z \frac{\partial T}{\partial x_i} + \frac{1}{2}\omega_i \frac{\partial T}{\partial z}\right) \ , \end{aligned} \tag{9}$$

where $T_k = T\boldsymbol{e}_z \cdot \boldsymbol{e}_k$, $S_i = [(\nabla\lambda) \times \nabla]_i$ and $d_{jk} = (\partial_j u_k + \partial_k u_j)/2$. The subscripts i, j and k vary among the Cartesian coordinates (x, y and z), and the summation conservation is applied to the repeating indices of j and k. The first three terms in the right-hand side of Eq.(9) represent the particle-induced effect, whereas the rest of the terms are the shear-induced and vorticity-induced effects. The above equation suggests the broad involvement of particle and rich mechanisms (via the variation of the thermal conductivity between the fluid and solid phases) for generating the horizontal temperature distribution and, in turn, the moment of buoyancy by Eq.(8).

The effect of the buoyancy force on the development of vortical structure is more focused with the

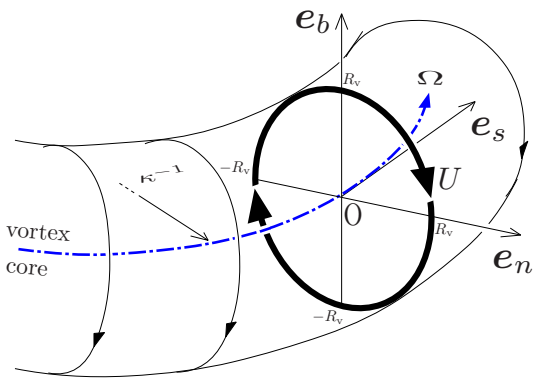

Figure 10: Schematic of a ring vortex and the local coordinates (n, s and b) at the origin. The curvature radius of the vortex core (the strength Ω) is κ^{-1} and the representative radius of the vortex is R_v.

transport equation of vorticity $\boldsymbol{\omega}$:

$$\frac{\mathrm{D}\boldsymbol{\omega}}{\mathrm{D}t} = \boldsymbol{\omega}\cdot\nabla\boldsymbol{u} + \nu\nabla^2\boldsymbol{\omega} + g\beta\nabla\times(T\boldsymbol{e}_z)\ . \tag{10}$$

Here, to describe the vortex in a Lagrangian way, vorticity distribution along the axisymmetric circular vortex core in the xy plane passing through the origin is considered. Figure 10 schematically illustrates the vortex and its core by a bold line and broken line, respectively. The curvature radius of the circular core is κ^{-1} and the representative radius of the vortex is R_v. In the following, s is the arc length along the vortex core, and n and b axes are taken to be perpendicular to the s axis. The n, s and b axes coincide with x, y and z axes at the origin, respectively. Then, the velocity and vorticity on the frame are described as follows:

$$\boldsymbol{u} = U_n\boldsymbol{e}_n + U_b\boldsymbol{e}_b,\quad \boldsymbol{\omega} = \Omega(n,b,t)\boldsymbol{e}_s\ .$$

Representing the vortex ring with the reduced degrees of freedom (i.e., Ω and κ) simplifies Eq.(10) into the following Lagrangian form:

$$\frac{\mathcal{D}\Omega}{\mathcal{D}t}\boldsymbol{e}_s - \kappa\Omega\frac{\partial s}{\partial t}\boldsymbol{e}_n = \nu(\nabla^2\Omega - \kappa^2\Omega)\boldsymbol{e}_s + g\beta\nabla\times(T\boldsymbol{e}_z)\ , \tag{11}$$

where

$$\frac{\mathcal{D}}{\mathcal{D}t} = \frac{\partial}{\partial t} + U_n\frac{\partial}{\partial n} + U_b\frac{\partial}{\partial b}\ . \tag{12}$$

Note that, by taking s_0 as the reference coordinate along the arc of the initial vortex core at $t = 0$ (the reference time), $\partial\boldsymbol{e}_s/\partial t = (\partial\boldsymbol{e}_s/\partial s_0)J^{-1}(\partial s/\partial t)$ follows, where $J\ (= \partial s/\partial s_0)$ is the Jacobian. However, focusing on a brief moment at around $t \sim \delta t \ll R_\mathrm{v}/U$, J is approximated to be unity. Therefore, in Eq.(11), the time derivative of $\boldsymbol{e}_s$ is treated as $\partial\boldsymbol{e}_s/\partial t \simeq (\partial\boldsymbol{e}_s/\partial s)(\partial s/\partial t) = -\kappa\boldsymbol{e}_n\partial s/\partial t$. Hereafter, to simplify the equation with low degrees of freedom, time-development of the vortex core and ring is constrained to the planar axisymmetric mode and smooth initial evolution: $\partial\kappa/\partial s = \partial\Omega/\partial s = \partial^2 s/\partial t^2 = 0$, $\Omega = \Omega(r,t)$, where r is the radius in the nb plane. Then, the time development of the curvature is discussed in the following. By applying the $\mathrm{D}/\mathrm{D}t$ operator to Eq.(11), and using Eq.(9) and $\partial\kappa/\partial n = -\kappa^2$, the $\boldsymbol{e}_n$-component of the vortex dynamics equation is described as:

$$\frac{\partial\kappa}{\partial t} + \sigma\kappa - U_n\kappa^2 - \nu\kappa^3 = -\left(\Omega\frac{\partial s}{\partial t}\right)^{-1}\mathbf{RHS}\cdot\boldsymbol{e}_n \tag{13}$$

where

$$\sigma = \frac{\nu\nabla^2\Omega}{\Omega} - 2\frac{g\beta}{\Omega}\frac{\partial T}{\partial n}\,, \tag{14a}$$

$$\mathbf{RHS}\cdot\boldsymbol{e}_i = \frac{g\beta}{\rho c}\left(\frac{\partial(S_iT_k)}{\partial x_k} - \frac{\partial(S_jT_j)}{\partial x_i}\right) + \frac{g\beta}{\rho c}\nabla^2\left[\lambda\nabla\times(T\boldsymbol{e}_z)\right]_i - g\beta\,\varepsilon_{ij3}d_{jk}\frac{\partial T}{\partial x_k}\,. \tag{14b}$$

Assuming that the κ^{-1} is much larger than R_v, the κ^2 and κ^3 terms in Eq.(13) are negligible. Then, the left-hand side of Eq.(13) exhibits that the curvature κ develops as $\exp(-\sigma\,t)$ (showing a stable/unstable trend depending on the sign of σ). Under an assumption that the Ω takes a convex and axisymmetric distribution in the nb plane, the first term in the right-hand side of Eq.(14a) is approximated as $-4/R_\mathrm{v}^2$. The second term of σ is originated from $\boldsymbol{e}_n\cdot(\nabla\times(T\boldsymbol{e}_z))$, and, for this term, the lower bound for the temperature gradient in the n direction is $-\Delta T/2R_\mathrm{v}$ for the case of Fig. 10. Finally, the diameter of the vortex is approximated to be the height of the computational domain, $H = 2R_\mathrm{v}$. Then, the characteristic time constant σ is estimated as follows:

$$\sigma \approx \frac{\nu}{H^2}\left(-16 + \chi\sqrt{\frac{\mathrm{Ra}}{\mathrm{Pr}}}\right)\,, \tag{15}$$

where $\chi = |\partial T/\partial n|/(\Delta T/H)$ varies between 0 and 1, depending on how violently the heat is transported from the bottom and top walls to the middle level ($z/H = 0.5$). Note that exactly the same σ-estimation as above also applies to a vortex counter-rotating with respect to the one depicted in Fig. 10. Considering that the present study is under $\mathrm{Ra} = 10^5$ and $\mathrm{Pr} = 1$, the strong convection induced by the highly-conductive particles would have a positive σ value, suggesting the possibility of a transformation of a ring vortex ($\kappa \neq 0$) to a line vortex ($\kappa \to 0$). A reverse process (i.e., from straight roll cell structure ($\kappa = 0$) to a ring vortex ($\kappa \neq 0$)) may not be simply described with a negative σ value: rather, negative σ exhibits a tendency to become a vortex ring of larger κ. However, the above analysis suggests the tendency only in a short moment at around $t \sim \delta t$, and a subsequent development of the vortex ring involves the non-linearity, which is eliminated in Eqs.(13) and (14).

Although the highly conductive particles are strong source of disturbance, a straight-roll cell could be a stable structure, unless the particles are transported by far to induce a different influential flow structure (e.g., turbulent regime under a higher Ra) or the particle-dispersed natural convection exhibits an intrinsically different type of stable flow structure (e.g., oscillation mode under a lower Ra [16]). Generally, the transition of the flow structure is dependent on the domain size, and studying the various transition scenarios caused by highly-conductive particles is the subject of ongoing study by the present authors. On the other hand, less-conductive particles are not as influential as the highly-conductive ones as to drastically change the flow structure by the thermally-associated effect, as will be observed in the next subsection.

4.4 Effect of the thermal conductivity ratio

The effect of the conductive and convective components of the heat fluxes on the vortical flow structure is discussed further by varying λ_s/λ_f.

Two cases of different thermal conductivity ratios $\lambda_s/\lambda_f = 10^0$ and 10^{-2} are chosen with keeping the other parameters and the conditions the same as the previous subsections. The instantaneous conductive and convective HFLs are shown in Fig. 11.

As the suspension is stirred by a point-source structure for both cases, the convective HFLs (bold line) run from the lower wall in the centre of the domain to the upper wall and go back to the lower wall. The weak temperature gradient in the vertical direction (shown by the colour contour in the vertical cross-sections in

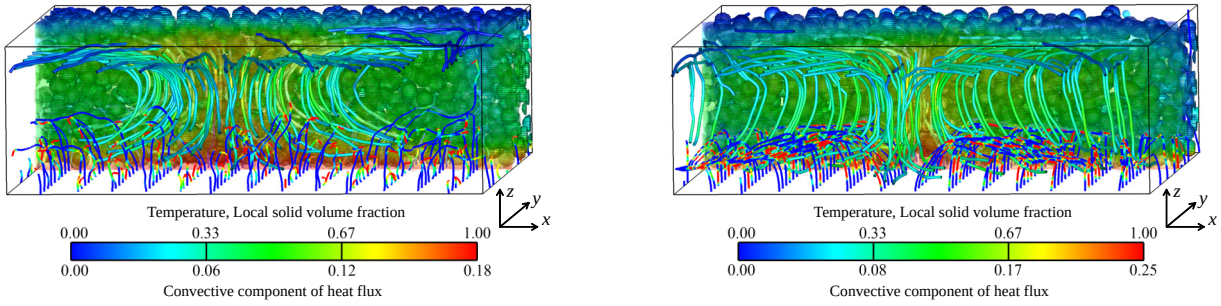

(a) $\lambda_s/\lambda_f = 10^{-2}$ (b) $\lambda_s/\lambda_f = 10^{0}$

Figure 11: Instantaneous heat flux lines of the conduction (thin line) and convection (bold lines) at $t\,U/H = 480$ for different particle conductivities of (a) $\lambda_s/\lambda_f = 10^{-2}$ and (b) 10^{0}. The colours on the conductive and convective HFLs are by the local solid volume fraction and the convective heat flux, respectively. The particles are only depicted in the rear half of the domain ($0.5 \leq y/W \leq 1$) and coloured by the local surface temperature.

Fig. 11 around the foot of the up-flow indicates the weakened conduction by the same mechanism as in Fig. 6. For both conductivity ratios, even with the relatively higher temperature gradient in the down-flow regions near the hot wall, the conductive HFLs (thin lines) mainly go through the fluid region due to the low thermal conductivity of the particles. The conductive HFLs deflect in the horizontal direction, suggesting that the heat from the hot wall is only diffused within a limited vertical level near the hot wall. Above the diffused-temperature region, both the poorly- and neutrally-conductive particles form a thermally inactive layer, where the horizontal temperature distribution by the conduction is weak. Eq.(15) shows that a small χ value evaluated at the vortex centre may yield a negative σ value, suggesting a persistent point-source/sink structure. Therefore, the particle-induced moment of buoyancy (Eq.(8)) will not be the primary mechanism for the formation of vortical flows for the case with the less-conductive particles.

This difference in the spatial extension of the conductive HFLs from the case of Figs.5(a) and 7(a), is reflected on the time-averaged Nusselt number, $\overline{\mathrm{Nu}}$. For $\lambda_s/\lambda_f = 10^{-2}$ and 10^{0}, $\overline{\mathrm{Nu}} = 1.9$ and 3.5, respectively, while the case of $\lambda_s/\lambda_f = 10^{2}$ shows $\overline{\mathrm{Nu}} = 5.9$. Here, the time-average is taken after $t\,U/H = 150$.

With the hindrance of the conduction by a large number of the low-conductivity particles, there is not sufficient heat supply for increasing the buoyancy force to overturn the local convection, suggesting that the convection-dominant mode of the heat transfer does not vary as much as that of the case of $\lambda_s/\lambda_f = 10^{2}$. This covers the view point of the previous study [17], and the present results provide more detailed information in the sense that the HFLs clearly show that the spatial extensions of the conductive and convective heat fluxes in the dense solid-dispersed media disturb and/or form a large-scale flow structure through the buoyancy force.

5 Conclusion

In the present study, the heat flux lines enabled investigation of the heat transfer paths in a dense particulate media containing finite-volume particles (i.e., non-point particle), and the effect of the local heat transfer on the formation and transition of the large-scale vortical structures was studied.

Through visualisation of the heat flux lines of the conductive and convective components, the cooperative effect of the conduction and convection was focused in a dense particle-dispersed natural convection

between two parallel plates. The results show that, for higher λ_s/λ_f, the local convection strengthens the conduction in the counter-convective direction by increasing the local temperature gradient in the vertical direction as well as the solid volume fraction near the hot wall. The local temperature distribution by the highly-conductive particles induces a large-scale vortical structure by the distribution of the moment of buoyancy.

A vortex model of reduced degree of freedom showed that the time-development of the large-scale vortical structure is determined by the balance between the transverse-gradient of buoyancy and the vorticity diffusion. The study also suggested that the highly-conductive particle exhibits rich mechanism (in comparison to the case with particles of low-conductivity or single-phase natural convection) for generating the horizontal temperature distribution and, in turn, the moment of buoyancy.

On the other hand, the less-conductive particles (i.e., $\lambda_s/\lambda_f = 10^0, 10^{-2}$) in a fluid were found to hinder the convective and conductive heat transfers by restricting the heat from the hot wall only to diffuse in the near region of the lower wall, giving rise not-sufficient heat to be transferred (to increase the buoyancy force) to overturn the suspension motion. Under the present Rayleigh number, the major heat transfer mode in the suspension was determined depending on the thermal conductivity ratio of the particle to the fluid and the bulk solid volume fraction, and the spatial extension of the heat flux lines (through the fluid, particle or inter-particle contacting site) has influenced the formation of the global flow structure in the inhomogeneous particulate media.

The present study showed that the observation of both conductive and convective heat flux lines was useful for understanding the finite-volume effect of the particles in dense particle-dispersed natural convection. Further, the effect of the cooperative effect of the two heat transfer modes on the development of large-scale vortical structures was revealed. The results will contribute to a fundamental and essential understanding of heat transfer in the solid-liquid two-phase flow.

Acknowledgements

This work is partly supported by Grant-in-Aid (B) No.16H04271 and No.17H03174 of the Japan Society for the Promotion of Science (JSPS).

Appendix A Numerical methods

For the governing equations (1), (2) and (3), numerical methods are briefly explained in this section.

Based on our original immersed solid method [18, 20], the procedure of the interaction between the fluid and particle is briefly explained in the following. In the method, one particle diameter is typically resolved more than 10 grid points. Hereafter, the cell partially occupied by the solid object is referred to as interfacial cell. The velocity in the interfacial cells is established by volume-averaging the fluid velocity and the particle velocity:

$$\boldsymbol{u} = (1-\alpha)\boldsymbol{u}_f + \alpha\boldsymbol{u}_s \,, \tag{A1}$$

where α is the local solid volume fraction and the subscript "s" denotes the solid phase. The velocity field

of the interface is assumed to obey Eq.(3) and the intermediate velocity field $\widehat{\boldsymbol{u}}$ is obtained as follows:

$$\widetilde{\boldsymbol{u}} = \boldsymbol{u}^n + \int_{t^n}^{t^{n+1}} \mathrm{d}t \left[-\nabla p + (\boldsymbol{u}\cdot\nabla)\boldsymbol{u} + \sqrt{\frac{\mathrm{Pr}}{\mathrm{Ra}}}\nabla^2\boldsymbol{u} - (T-T_0)\boldsymbol{j} \right] , \tag{A2}$$

$$\nabla^2\phi = \frac{\nabla\cdot\widetilde{\boldsymbol{u}}}{\Delta t} , \tag{A3}$$

$$\widehat{\boldsymbol{u}} = \widetilde{\boldsymbol{u}} - \nabla\phi\,\Delta t , \tag{A4}$$

where $\Delta t = t^{n+1} - t^n$ is the time increment. In this paper, the time-integrations of the convective and viscous terms in Eq.(A2) are carried out by the second-order Adams-Bashforth and Crank-Nicolson methods, respectively. The momentum interaction term between the phases is modeled to enforce the rigid-object velocities at the cells inside the solid phase (as well as the no-slip condition at the object surface) and given in the following form [20]:

$$\boldsymbol{f}_I^n = \frac{\alpha(\boldsymbol{u}_s^n - \widehat{\boldsymbol{u}})}{\Delta t} , \tag{A5}$$

The velocity and pressure fields complete the time update to the next time level $(n+1)$ as:

$$\boldsymbol{u}^{n+1} = \widehat{\boldsymbol{u}} + \boldsymbol{f}_I^n\,\Delta t , \tag{A6}$$

$$p^{n+1} = p^n + \phi . \tag{A7}$$

The motion of the solid particle is calculated in the Lagrangian frame. The translating and angular velocities of the particle are updated as follows:

$$\boldsymbol{u}_s^{n+1} = \boldsymbol{u}_s^n + m_s^{-1}\int_{t^n}^{t^{n+1}} \mathrm{d}t \int_{V_s} (-\rho_f \boldsymbol{f}_I)\,\mathrm{d}V_s , \tag{A8}$$

$$\boldsymbol{\omega}_s^{n+1} = \boldsymbol{\omega}_s^n + \boldsymbol{I}^{-1}\cdot\int_{t^n}^{t^{n+1}} \mathrm{d}t \int_{V_s} \boldsymbol{R}_s \times (-\rho_f \boldsymbol{f}_I)\,\mathrm{d}V_s , \tag{A9}$$

where m_s is the particle mass, V_s the volume enclosing the particle, $\boldsymbol{\omega}_s$ the angular velocity vector, $\boldsymbol{I}_s$ the inertia tensor of the particle and $\boldsymbol{R}_s$ the radial vector from the particle center to the interfacial cell. The location of the individual particle is updated by the Crank-Nicolson method. The detail of the above algorithm is found in the Refs.[18, 20].

The heat transfer at the interfacial cell is calculated with the method used in Refs. [16, 18]. The interfacial heat flux model on a discretized field is summarized in the following. In the interfacial cell (cell indices i, j and k), the discretized temperature gradient is decomposed into the normal direction:

$$(\boldsymbol{n}\cdot\nabla T|_{ijk})\,\boldsymbol{n} , \tag{A10}$$

and the tangential direction:

$$\nabla T|_{ijk} - (\boldsymbol{n}\cdot\nabla T|_{ijk})\,\boldsymbol{n} , \tag{A11}$$

where $\boldsymbol{n}$ represents the unit vector in the outward normal direction of the particle surface. In the following, λ_h and λ_a are the thermal conductivities in the interfacial cell in the normal and tangential directions, respectively:

$$\frac{1}{\lambda_h} = \frac{1-\alpha}{\lambda_f} + \frac{\alpha}{\lambda_s} , \tag{A12}$$

$$\lambda_a = (1-\alpha)\lambda_f + \alpha\lambda_s , \tag{A13}$$

where λ_f and λ_s are the thermal conductivities of the fluid and solid phases. By multiplying the above thermal conductivities to Eqs. (A10) and (A11), the local heat flux at the interfacial cell is constructed as the sum of those in the respective directions:

$$-\boldsymbol{q}_I = \lambda_h(\boldsymbol{n}\cdot\nabla T|_{ijk})\boldsymbol{n} + \lambda_a\big(\nabla T|_{ijk} - (\boldsymbol{n}\cdot\nabla T|_{ijk})\boldsymbol{n}\big)\ . \tag{A14}$$

The derivation and validations are detailed in Refs. [16, 17]. Note that the above Eulerian treatment of the heat flux at the interfacial cells shows good compatibly with the immersed solid method, Eqs.(A1)-(A9). A further advanced treatment of the interfacial heat flux is found in Ref. [22] with the special emphasis on the consistency of the discretized form of the heat flux at the interfacial cell.

The thermal contact resistance is calculated by the method developed in Ref. [18] that takes account of the effect of the heat flux inside the individual particles on the contact resistance. In the following, only the result is briefly summarized. The contact site of a pair of solid objects is modeled as a constricted cylinder immersed in a fluid. By solving the steady heat conduction equations in the cylinder and the surrounding fluid region, the "equivalent length" of the thermal resistance at the constriction, l_R, is calculated as:

$$\frac{l_R}{r_2} = 2\left(\frac{D_1}{D_0} + \frac{z_1}{r_2}\right)\ ,$$

where z_1 is the half height of the constriction, r_2 the radius of the cylinder, $D_i\ (i = 0, 1)$ the determinants of the matrices comprising the coefficients of the eigenfunction decomposition (i.e., using Bessel functions) of the temperature, as detailed in Ref. [18]. Then, the heat flux $\boldsymbol{q}_I^C$ at the contact site is represented as:

$$-\boldsymbol{q}_I^C = \lambda_h^C\left(\left(\boldsymbol{n}\cdot\nabla T|_{ijk}\right)\boldsymbol{n}\right) + \lambda_a^C\left(\nabla T|_{ijk} - \left(\boldsymbol{n}\cdot\nabla T|_{ijk}\right)\boldsymbol{n}\right)\ , \tag{A15}$$

where

$$\lambda_h^C = \left(1 - \frac{2z_1}{\Delta} + \frac{l_R}{\Delta}\right)^{-1}\lambda_s\ , \tag{A16}$$

$$\lambda_a^C = \left(1 - \frac{2z_1}{\Delta}\right)\lambda_s\ . \tag{A17}$$

The above equation (A15) is apparently the same form as Eq. (A14), and both the thermal contact resistance and the temperature distribution inside individual particles are considered for the heat flux across the contact site of the particles.

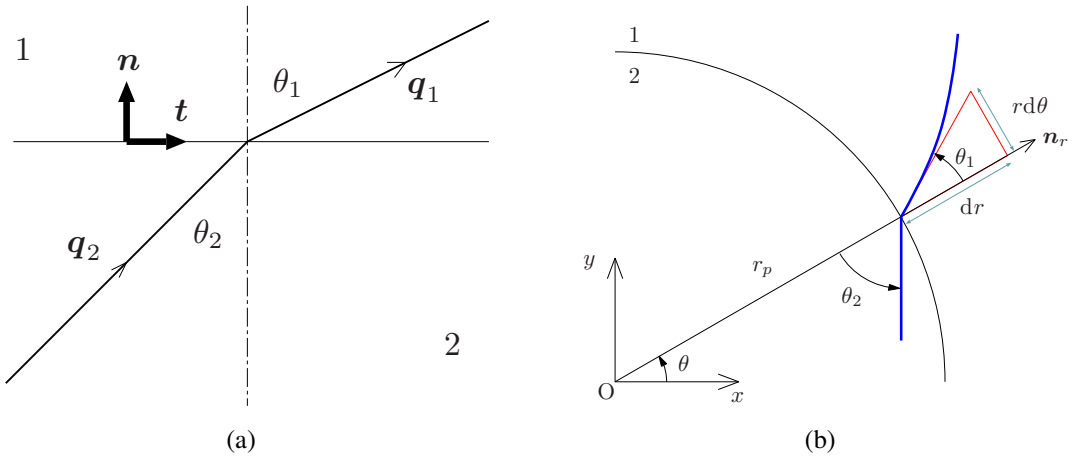

Figure B1: Schematic of the interface between the phases 1 and 2.

Appendix B Thermally-influential regions by two particles

B.1 Boundary conditions

Let us consider a thermal flux at an interface of the phases 1 and 2, as schematically shown in Fig. B1(a).

With no heat source on the interface, the heat flux $\boldsymbol{q}_i$ $(i = 1, 2)$ in the normal direction is continuous:

$$\boldsymbol{q}_1 \cdot \boldsymbol{n} = \boldsymbol{q}_2 \cdot \boldsymbol{n} \,,$$

where $\boldsymbol{n}$ is the unit normal vector from the phases 2 to 1. On the other hand, assuming the coincidence of the temperatures of the two phases at the interface, the tangential components of the temperature gradients are the same at the interface:

$$(\nabla T_1) \cdot \boldsymbol{t} = (\nabla T_2) \cdot \boldsymbol{t} \,,$$

where $\boldsymbol{t}$ is the unit tangential vector. Hereafter, we apply the Fourier law for the heat flux. By setting the angles between $\boldsymbol{q}_i$ $(i = 1, 2)$ and $\boldsymbol{n}$ to θ_i $(i = 1, 2)$, the above equations read as follows:

$$\lambda_1 |\nabla T_1| \cos\theta_1 = \lambda_2 |\nabla T_2| \cos\theta_2 \tag{B18}$$

$$|\nabla T_1| \sin\theta_1 = |\nabla T_2| \sin\theta_2 \,, \tag{B19}$$

where λ_i $(i = 1, 2)$ is the heat conductivity of the phase i. Then the following interfacial condition is obtained:

$$\frac{\tan\theta_1}{\tan\theta_2} = \frac{\lambda_1}{\lambda_2} \,. \tag{B20}$$

B.2 Complex-variable function for heat flux

Here we study the conductive heat flux in and around a cylindrical particle (radius r_p) fixed in a uniform heat flux field. The external uniform heat flux is in the y direction and normal to the axis of the cylinder. Inside the particle, the heat flux is parallel with the direction of the external heat flux, although the magnitude of the heat fluxes changes inside and outside the cylinder.

Hereafter, the set-up is restricted to two-dimensions. The heat flux $\boldsymbol{q}$ is deduced from a complex-variable function

$$W(z) = iV\left(z + \frac{\eta}{z}\right) . \tag{B21}$$

where i is the imaginary unit, η is a constant and V is the magnitude of the external uniform heat flux. Note that the form of V is not very relevant to the discussion in this appendix, but it corresponds to the heat flux in a region far away from the cylinder, $V = \Delta T/L$, in the Rayleigh-Bénard problem of the closed container.

In the following, we determine η that satisfies Eq.(B20). The radial and azimuthal components of the heat flux, q_r and q_θ, are given as follows:

$$\begin{aligned} q_r - iq_\theta &= \frac{\mathrm{d}W}{\mathrm{d}z}e^{i\theta} \\ q_r &= -V\left(1 + \frac{\eta}{r^2}\right)\sin\theta\,, \quad q_\theta = V\left(-1 + \frac{\eta}{r^2}\right)\cos\theta\,. \end{aligned} \tag{B22}$$

For the configuration in Fig.B1(b), the tangent of θ_1 is written with the heat fluxes in the normal and tangential directions:

$$\tan\theta_1 = \left.\frac{r\mathrm{d}\theta}{\mathrm{d}r}\right|_{r=r_p} = \left.\frac{q_\theta}{q_r}\right|_{r=r_p} = \left.\frac{V\left(-1+\eta r^{-2}\right)\cos\theta}{-V\left(1+\eta r^{-2}\right)\sin\theta}\right|_{r=r_p} = \frac{r_p^2 - \eta}{r_p^2 + \eta}\cot\theta\,. \tag{B23}$$

Inside the particle, on the other hand, the heat flux is parallel with the external heat flux, yielding the following condition:

$$\tan\theta_2 = \tan\left(\frac{\pi}{2} - \theta\right) = \cot\theta\,. \tag{B24}$$

Substituting Eqs.(B23) and (B24) into Eq.(B20) determine η as follows:

$$\eta = \frac{-\lambda_1 + \lambda_2}{\lambda_1 + \lambda_2} r_p^2$$

Hereafter, we replace the heat conductivities as $\lambda_1 \to \lambda_f,\ \lambda_2 \to \lambda_s$ to match the notation in the present paper, and a short-hand notation $\Lambda = \lambda_s/\lambda_f$ is introduced, then the above η is simplified to the following form:

$$\eta = \frac{\Lambda - 1}{\Lambda + 1} r_p^2\,. \tag{B25}$$

The above result suggests that the non-uniform media (i.e., phases 1 and 2 in the present set-up) satisfies the interfacial condition (B20) and enforces the constant η to the above form, which is different from the complex-variable analysis of a potential flow.

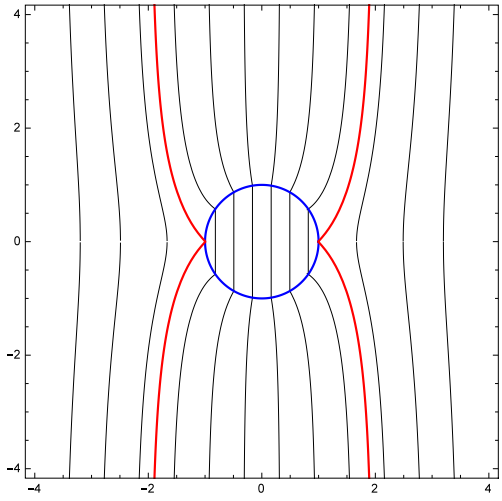

Figure B2: One example of an hour-glass shape of the limiting heat flux lines (represented in red) obtained under $r_p = 1, V = 1$ and $\lambda_s/\lambda_f = 10^2$.

B.3 Limiting heat flux lines in a single-particle system

Eq.(B21) yields a heat-flux function (corresponding to a stream function) as:

$$\Psi(x,y) = \mathrm{Im}[W] = V\left(x + r_p^2 \frac{\Lambda-1}{\Lambda+1}\frac{x}{x^2+y^2}\right) .$$

Note that $\Psi = \mathrm{Const.}$ means a heat flux line. Hereafter, we refer to the HFL passing through the points $(x,y) = (\pm r_p, 0)$ the limiting HFL. The limiting HFLs have the following values of Ψ:

$$\Psi_{\pm r_p} = \pm V r_p \left(\frac{\Lambda-1}{\Lambda+1} + 1\right) . \tag{B26}$$

The form of the limiting HFL is obtained by solving $\Psi(x,y) = \Psi_{\pm r_p}$ and given as follows:

$$y\left(x;\Psi_{+r_p}\right) = \pm\sqrt{x(r_p-x)}\frac{\sqrt{r_p(1-\Lambda)+x(1+\Lambda)}}{\sqrt{-2r_p\Lambda+x(1+\Lambda)}} , \tag{B27}$$

$$y\left(x;\Psi_{-r_p}\right) = \pm\sqrt{x(r_p+x)}\frac{\sqrt{r_p(1-\Lambda)-x(1+\Lambda)}}{\sqrt{2r_p\Lambda+x(1+\Lambda)}} . \tag{B28}$$

Figure B2 shows the heat flux lines ($\Psi = \mathrm{Const.}$) and the above limiting HFLs are highlighted in red.

The inverse functions of Eqs.(B27)(B28) are denoted as $x\left(y;\Psi_{\pm r_p}\right)$, respectively. Under $y \to \pm\infty$, those inverse functions have the asymptotic lines:

$$\lim_{|y|\to\infty} x\left(y;\Psi_{\pm r_p}\right) = \pm\frac{2\Lambda r_p}{1+\Lambda} . \tag{B29}$$

In this limit, the x-distance between the two limiting HFLs, b, is determined as:

$$\lim_{|y|\to\infty} b = \frac{2\Lambda}{1+\Lambda}D_p \qquad (D_p = 2r_p) . \tag{B30}$$

Hereafter, we refer to this x-distance the asymptotic width of the limiting HFLs (or simply "width"). Note that the width of the limiting HFLs are independent of V. The asymptotic width exhibits a monotonous increase with respect to $\Lambda\,(>0)$, and in the limit of $\Lambda \to \infty$, we obtain

$$\lim_{\Lambda\to\infty} \lim_{|y|\to\infty} b = 2D_p\,, \tag{B31}$$

suggesting that asymptotic width of the limiting HFLs is no larger than $2D_p$.

In the present problem set-up of particle-dispersed Rayleigh-Bénard convection, the domain size is finite (unlike the above problem set-up). However, if the domain size is sufficiently large in comparison to a particle diameter and the particle position is not too close to the heated/cooled wall, the width of the limiting HFLs of a highly conductive particle is not very different from $2D_p$, and an approximate modeling with this characteristic length is effective. In the following, heat flux lines in a two-particle system is estimated based on the above characteristic width.

B.4 Two-particle system

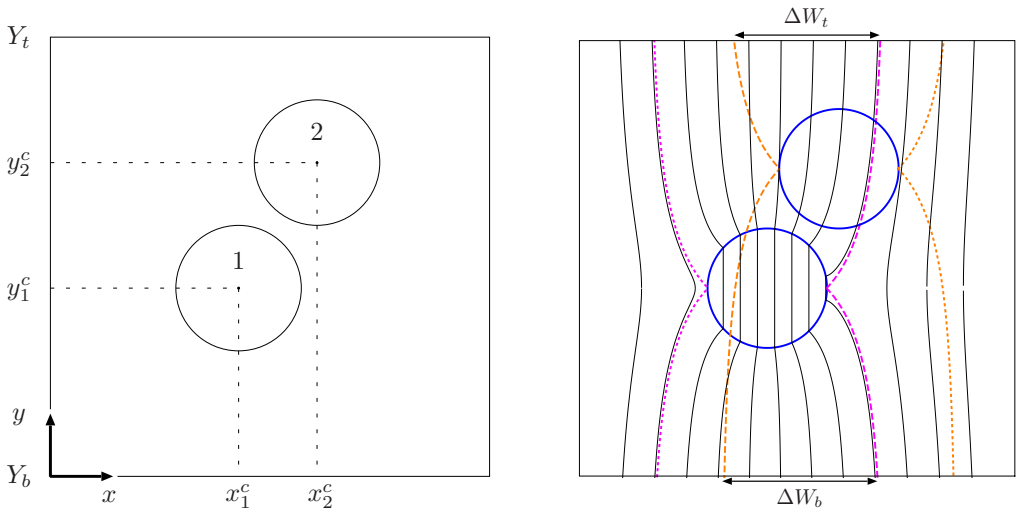

(a) (b)

Figure B3: Schematics of a two-particle system. The center of one particle is placed inside the region enclosed by the limiting heat flux lines of the other particle.

In the following, we look into a two-particle system, and particularly focus on a configuration that one particle center is inside the region enclosed by the limiting HFLs of the other particle. Figure B3 illustrates this situation.

As Fig. B3(b) shows, the inner pair of the limiting HFLs of the particles 1 and 2 (represented by the pair of broken lines) are defined as "thermally-influential region". Then, the width of the influential region on the upper boundary (located at $y = Y_t$) is denoted as ΔW_t, and similarly, ΔW_b is the width of the influential region on the lower boundary ($y = Y_b$). The widths are obtained as follows:

$$\text{Width on top-plane}(y = Y_t): \quad \Delta W_t = \frac{F(B_1^t, B_3^t) + 4r_p\Lambda - 3\Lambda x_2^c - 3x_2^c + G(B_2^t, B_4^t)}{3(\Lambda+1)}\,,$$

$$\text{Width on bottom-plane}(y = Y_b): \quad \Delta W_b = \frac{F(B_1^b, B_3^b) + 4r_p\Lambda - 3\Lambda x_2^c - 3x_2^c + G(B_2^b, B_4^b)}{3(\Lambda+1)}\,,$$

where the functions F, G are given as:

$$F(B_1, B_3) = -\sqrt[3]{\sqrt{B_1} - r_p\Lambda\left(r_p^2\left(5\Lambda^2+27\right)+6B_3\right)} + \frac{B_3}{\sqrt[3]{\sqrt{B_1} - r_p\Lambda\left(r_p^2\left(5\Lambda^2+27\right)+6B_3\right)}}$$

$$G(B_2, B_4) = +\sqrt[3]{\sqrt{B_2} + r_p\Lambda\left(r_p^2\left(5\Lambda^2+27\right)+6B_4\right)} - \frac{B_4}{\sqrt[3]{\sqrt{B_2} + r_p\Lambda\left(r_p^2\left(5\Lambda^2+27\right)+6B_4\right)}}$$

and B_j^d $(j = 1, \cdots, 4, d = b, t)$ are as follows:

$$\begin{aligned}
B_1^d &= r_p^2\Lambda^2\left(r_p^2\left(\Lambda^2-9\right) - 18(\Lambda+1)^2(Y_d - y_2^c)^2\right)^2 - \left(r_p^2\left(\Lambda^2+3\right) - 3(\Lambda+1)^2(Y_d-y_2^c)^2\right)^3 \\
B_2^d &= -27(\Lambda+1)^2\left(r_p^6(\Lambda-1)^2 + r_p^4\left(\Lambda^4 - 14\Lambda^2 - 3\right)Y_d^2 - r_p^2(\Lambda+1)^2\left(11\Lambda^2-3\right)Y_d^4 - (\Lambda+1)^4 Y_d^6\right) \\
B_3^d &= 3(\Lambda+1)^2(Y_d-y_2^c)^2 - r_p^2\left(\Lambda^2+3\right) \\
B_4^d &= 3(\Lambda+1)^2 Y_d^2 - r_p^2\left(\Lambda^2+3\right)
\end{aligned}$$

The difference in the widths of the heat flux lines is introduced as:

$$\Delta W = \Delta W_b - \Delta W_t \, .$$

Here, to highlight the effects of the parameters on the widths on the top and bottom walls, the second particle is assumed to be located at slightly higher level than the first particle as

$$y_2^c = 2r_p(1+\alpha)$$

where $\alpha\,(>0)$ is a non-dimensional parameter.

Now, we set up a configuration that Particle 1 is fixed close to the upper wall and that Particle 2 is located inside the upper side of the thermally-influential region of Particle 1. For this, we set the parameters as follows: $y_1^c - Y_b = 35r_p$, $y_2^c - y_1^c = 3r_p + 2\alpha r_p$ and $Y_t - y_2^c = 2r_p(1-\alpha)$, which assumes the same ratio of the particle size to the side length of the domain, $Y_t - Y_b = 40r_p\,(= H)$.

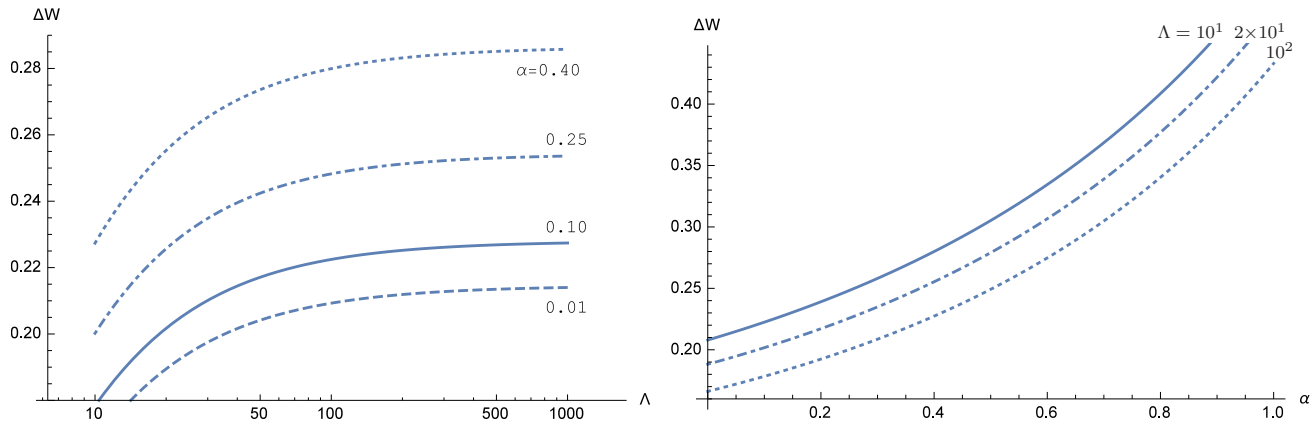

(a) $\alpha = 0.01,\ 0.1,\ 0.25,\ 0.40$ (b) $\Lambda(=\lambda_s/\lambda_f) = 10^1,\ 2{\times}10^1,\ 10^2$

Figure B4: The dependences of ΔW on (a) Λ for different α values and on (b) α for different Λ values.

Figure B4 summarizes the dependences of ΔW on Λ and α: ΔW takes positive values and the value increases as α is increases in the range of $10^1 \leq \Lambda \leq 10^3$. Similar dependence is observed for different configurations with two particles inside the limiting HFLs of the other. The result suggests that the thermally-influential region by two particles shrinks in the upper side of the particles, resulting in focusing effect of the heat in a upper side, when the particles are near the upper wall. If not near the wall, the widths ΔW_d $(d = b, t)$ would be comparable due to the symmetry of the problem.

However, with more number of particles, this effect will be more complex, and temperature is expected to distribute unevenly near the top wall. The fluctuation of temperature eventually causes distribution of the first-order moment of buoyancy ($\boldsymbol{F}_\mathrm{b} = \boldsymbol{g}\beta(T - T_0)$), causing the up-flow/down-flow region to move horizontally. Here, we utilise the following identify [23]:

$$\int_V \boldsymbol{x} \times \boldsymbol{f}\,\mathrm{d}V = -\frac{1}{2}\int_V |\boldsymbol{x}|^2 \nabla \times \boldsymbol{f}\,\mathrm{d}V - \frac{1}{2}\int_S |\boldsymbol{x}|^2 \boldsymbol{f} \times \boldsymbol{n}\,\mathrm{d}S \tag{B32}$$

where $\boldsymbol{x}$ is the direction vector, $\boldsymbol{f}$ an arbitrary vector, $\boldsymbol{n}$ the outward normal vector on the boundary. By substituting $\boldsymbol{f}$ with $\boldsymbol{F}_\mathrm{b}$, the following equation explains the moment of buoyancy by the temperature distribution in a horizontal plane as:

$$\int \boldsymbol{x} \times \boldsymbol{F}_\mathrm{b}\,\mathrm{d}V \;\; = \;\; -\frac{g\beta}{2}\int_V |\boldsymbol{x}|^2 \nabla \times (T\boldsymbol{e}_z)\,\mathrm{d}V \tag{B33}$$

assuming that the normal vectors at the top and bottom boundaries is parallel with the buoyancy force.

References

[1] Murray, D.B. and Fitzpatrick, J.A., Heat transfer in a staggered tube array for a gas-solid suspension flow, *Journal of Heat Transfer*, Vol. 113(4), pp. 865-873, 1991.

[2] Mansoori, Z., Saffar-Avval, M., Basirat Tabrizi, H. and Ahmadi, G., Experimental study of turbulent gas-solid heat transfer at different particles temperature, *Experimental Thermal and Fluid Science*, Vol. 28, pp. 655-665, 2004.

[3] Radmila, G.G., Nevenka, B.V., Zeljko, G. and Zorana, A., Wall-to-bed heat transfer in vertical hydraulic transport and in particulate fluidized beds, *International Journal of Heat and Mass Transfer*, Vol. 51, pp. 5942-5948, 2008.

[4] Zuber, N., On the dispersed two-phase flow in the laminar flow regime, *Chemical Engineering Science*, Vol. 19, pp. 897-917, 1964.

[5] McLaughlin, J.B., Numerical computation of particles-turbulence interaction, *International Journal of Multiphase Flow*, Vol. 20, pp. 211-232, 1994.

[6] Hu, H.H., Direct simulation of flows of solid-liquid mixtures, *International Journal of Multiphase Flow*, Vol. 22, pp. 335-352, 1996.

[7] Michaelides, E.E., Heat transfer in particulate flows, *International Journal of Heat and Mass Transfer*, Vol. 29, pp. 265-273, 1986.

[8] Murray, D.B. and Fitzpatrick, J.A., The effect of solid particles on crossflow heat transfer in a tube array, *Experimental Thermal and Fluid Science*, Vol. 5, pp. 188-195, 1992.

[9] Murray, D.B., Local enhancement of heat transfer in a particulate cross flow — I, *International Journal of Multiphase Flow*, Vol. 20, pp. 493-504, 1994.

[10] Avila, R. and Cervantes, J., Analysis of the heat transfer coefficient in a turbulent particle pipe flow, *International Journal of Heat and Mass Transfer*, Vol. 38, pp. 1923-1932, 1995.

[11] Mansoori, Z., Saffar-Avval, M., Basirat Tabrizi, H., Ahmadi, G. and Lain, S., Thermo-mechanical modeling of turbulent heat transfer in gas-solid flows including particle collisions, *International Journal of Heat and Fluid Flow*, Vol. 23, pp. 792-806, 2002.

[12] Mansoori, Z., Saffar-Avval, M., Basirat Tabrizi, H., Dabir, B. and Ahmadi, G., Inter-particle heat transfer in a riser of gas-solid turbulent flows, *Powder Technology*, Vol. 159, pp. 35-45, 2005.

[13] McKenna, T.F., Spitz, R. and Cokljat, D., Heat transfer from catalysts with computational fluid dynamics, *Reactors, Kinetics, and Catalysis*, Vol. 45, No.11, pp.2392-2410, 1999.

[14] Nijemeisland, M. and Dixon, A.G., CFD study of fluid flow and wall heat transfer in a fixed bed of spheres, *AIChE.* Vol. 50 No.5, pp.906-921, 2004.

[15] McKenna, T.F., DuPuy, J. and Spitz, R., Modeling of transfer phenomena on heterogeneous Ziegler catalysts: Differences between theory and experiment in olefin polymerization (an introduction), *Journal of Applied Polymer Science*, Vol. 57, Issue 3, pp.371-384, 1995.

[16] Takeuchi, S., Tsutsumi, T. and Kajishima, T., Effect of temperature gradient within a solid particle on the rotation and oscillation modes in solid-dispersed two-phase flows, *International Journal of Heat and Fluid Flow*, Vol. 43, pp. 15-25, 2013.

[17] Tsutsumi, T., Takeuchi, S. and Kajishima, T., Heat transfer and particle behaviours in dispersed two-phase flow with different heat conductivities for liquid and solid, *Flow, Turbulence and Combustion*, Vol. 92, Issue 1-2, pp. 103-119, 2014.

[18] Takeuchi, S., Tsutsumi, T., Kondo, K., Harada, T., and Kajishima, T., Heat transfer in natural convection with finite-sized particles considering thermal conductance due to inter-particle contacts, *Computational Thermermal Sciences: An International Journal*, Vol. 7, pp. 385-404, 2015.

[19] Gu, J., Takeuchi, S. and Kajishima, T., Influence of rayleigh number and solid volume fraction in particle-dispersed natural convection, *International Journal of Heat and Mass Transfer*, Vol. 120, pp.250-258, 2018.

[20] Kajishima, T. and Takiguchi, S., Interaction between particle clusters and particle-induced turbulence, *International Journal of Heat Fluid Flow*, Vol. 23, pp. 639-646, 2002.

[21] Tsuji, Y., Kawaguchi, T. and Tanaka, T., Discrete particle simulation of two-dimensional fluidized bed, *Powder Technology*, Vol. 77, pp. 79-87, 1993.

[22] Sato, N., Takeuchi, S., Kajishima, T., Inagaki, M. and Horinouchi, N., A consistent direct discretization scheme on Cartesian grids for convective and conjugate heat transfer, *Journal of Computational Physics*, Vol. 321, pp.76-104, 2016.

[23] Saffman, P.G., *Vortex Dynamics*, Cambridge University Press, 1995.